Robust Gust Load Alleviation Control using Disturbance Observer for Generic Flexible Wing Aircraft in Cruising Condition*

Seung Jae Lee[1], Kelley E. Hashemi[2], Michael C. Drew[2], Nhan T. Nguyen[2] and H. Jin Kim[1]

***Abstract*— This paper deals with robust gust load alleviation control design for a flexible wing aircraft in cruising condition. Using an array of control surfaces called the Variable Camber Continuous Trailing Edge Flap, the gust load alleviation controller minimizes the structural load on the aircraft wing induced by a gust disturbance. The control terms are separated into two channels, rigid and elastic control input. Only the elastic control input is used for gust load alleviation while rigid control input is reserved for fundamental trajectory-level flight control. Utilizing equivalent input disturbance theory, the virtual input disturbance is calculated and compensated for by a disturbance observer robust control algorithm. Simulation results are provided with detailed analysis, proving the validity of the proposed method.**

I. INTRODUCTION

Use of composite materials in aerospace applications is becoming increasingly common due to their lightweight but high-strength mechanical properties. Aircraft wings can be constructed of composite materials to offer reduced weight but results in a more flexible structure. This flexibility introduces the possibility of deliberately modifying the shape of the wing for flight performance tasks such as drag reduction and increased fuel efficiency [1]. However, flexibility of the aircraft wing also increases vulnerability to undesirable aeroservoelastic behavior like flutter and poor disturbance rejection. Therefore, active control is necessary not only to improve performance of flexible wing aircraft, but to guarantee structural stability as well. Here, a gust load alleviation (GLA) control design is investigated as a means to improve the flexible aircraft's wind gust disturbance rejection capability.

Many GLA control designs for flexible wing aircraft have been proposed. Some designs utilize optimal control-based GLA where state-stabilizing controllers can be generated for multi-input multi-output (MIMO) plants [2],[3],[4]. Adaptive control-based GLA designs are also widespread due to anticipated aeroelastic model uncertainties. By constantly updating the system parameters with adaptive laws, the closed-loop performance during operation can be improved [5],[6]. However, since many disturbances contain fast-changing dynamic components for which adaptive control techniques would require prohibitively high learning rates, some researchers have tried to address the problem with robust control techniques that provide faster reaction to mitigate unknown disturbances [7],[8].

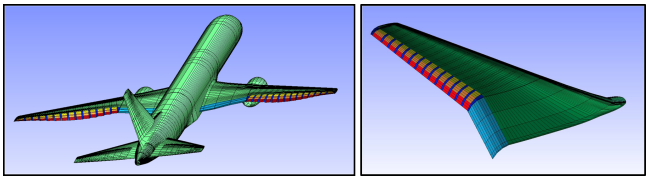

Fig. 1. Flexible wing aircraft with variable camber continuous trailing edge flap.

Among the numerous robust control algorithms, the disturbance observer (DOB) is well suited to deal with the specifics of the GLA problem. Notably, the DOB is an inner-loop controller that handles not only external disturbances but also plant model uncertainties [9]. The plant with DOB structure behaves like a nominal plant from the perspective of the outer-loop controller [10]. As our goal with GLA is to make the imperfectly known plant with disturbances act as a designated nominal plant, the DOB is an appropriate choice to obtain the performance desired from a GLA controller.

In this paper, we present a DOB robust controller design adapted for use as a GLA controller at cruise conditions. The goals of the GLA controller in this paper are to

- Reduce wing root bending moment
- Regulate elastic states of the system (flutter suppression).

Note that minimization of wing root bending moment is used as a stand-in performance metric for load minimization as has been done in previous investigations [5]. The proposed GLA design is demonstrated in simulation using the Generic Transport Model (GTM) equipped with wing-shaping actuators collectively known as the Variable Camber Continuous Trailing Edge Flap (VCCTEF). A detailed description of the VCCTEF mechanism can be found in [11], and the VCCTEF actuation system used here is illustrated in Fig. 1. The VCCTEF actuation system consists of an array of flaps where adjacent flaps are joined together by an elastomer transition material (blue inserts in Fig. 1) to create a continuous trailing edge. Due to the presence of the transition material, the relative angle between adjacent flaps is limited to 2°, while absolute deflection limits for each flap are $\pm 10^\circ$. We aim

*This work was supported by the Robotics Core Technology Development Project (10080301) funded by the Ministry of Trade, Industry and Energy (MoTIE, Korea), the National Research Foundation of Korea (NRF) grant (2014M1A3A3A02034854) and the program of National Space Laboratory (2014M1A3A3A02034856) funded by the Ministry of Science, ICT and Future Planning.

[1]Seung Jae Lee and H. Jin Kim are with the Department of Mechanical and Aerospace Engineering and Institute of Advanced Aerospace Technology (IAAT), Seoul National University, Gwanak-gu, Seoul, Korea sjlazza@snu.ac.kr, hjinkim@snu.ac.kr

[2]Kelley E. Hashemi, Michael C. Drew, and Nhan T. Nguyen are with the Intelligent Systems Division, NASA Ames Research Center, Moffett Field, CA 94035, USA kelley.e.hashemi@nasa.gov, michael.c.drew@nasa.gov, nhan.t.nguyen@nasa.gov

to achieve both of the stated GLA goals while adhering to actuation limitations.

The paper is organized as follows: In section II, the mathematical representation of GTM is covered. Including the DOB implementation process, the control strategies for GLA are described in section III. In section IV, we explain the design guidelines for the Q-filter which plays an important role in both stability and performance of the DOB algorithm. The GTM simulation results for the proposed GLA control algorithm are discussed in section V.

II. MODELING

A. Nominal Aeroservoelastic State-Space Model of GTM

The linearized, longitudinal plant dynamics of the flexible wing GTM, trimmed at mid-cruise flight conditions, can be written as

$$\begin{bmatrix}\dot{x}_r\\ \dot{x}_e\end{bmatrix} = \begin{bmatrix}A_{rr} & A_{re}\\ A_{er} & A_{ee}\end{bmatrix}\begin{bmatrix}x_r\\ x_e\end{bmatrix} + \begin{bmatrix}B_{rr} & B_{re}\\ B_{er} & B_{ee}\end{bmatrix}\begin{bmatrix}u_r\\ u_e\end{bmatrix} \quad (1)$$

where $*_r$ and $*_e$ represent rigid and elastic terms respectively. Rigid terms are associated with the aircraft's rigid body dynamics while the elastic terms are related to the aircraft's elastic modes. The matrices $A \in \Re^{n_x \times n_x}$ and $B \in \Re^{n_x \times n_u}$ are assumed to be known where n_x and n_u denote the dimension of states and inputs respectively. The vector $x_r \in \Re^{n_{x_r}}$ is composed of measurable rigid states, but components of $x_e \in \Re^{n_{x_e}}$ are unmeasurable and should be estimated. Note that $n_x = n_{x_r} + n_{x_e}$. Estimation of x_e is performed by

$$\dot{\hat{x}}_e = \begin{bmatrix}A_{er} & A_{ee}\end{bmatrix}\begin{bmatrix}x_r\\ \hat{x}_e\end{bmatrix} + \begin{bmatrix}B_{er} & B_{ee}\end{bmatrix}\begin{bmatrix}u_r\\ u_e\end{bmatrix} + L(y-\hat{y}) \quad (2)$$

where L represents the state observer's Kalman gain and $y \in \Re^{n_y}$ the vertical acceleration data measured by an array of n_y wing-mounted accelerometers [12]. The estimated output $\hat{y}$ is formed as

$$\hat{y} = \begin{bmatrix}C_r & C_e\end{bmatrix}\begin{bmatrix}x_r\\ \hat{x}_e\end{bmatrix} + \begin{bmatrix}D_r & D_e\end{bmatrix}\begin{bmatrix}u_r\\ u_e\end{bmatrix} \quad (3)$$

where $C \in \Re^{n_y \times n_x}$ and $D \in \Re^{n_y \times n_u}$ are known.

Wing root bending moment $M_y \in \Re^1$ is measurable via a strain gauge attached near the wing root, but an estimate can also be constructed as

$$\hat{M}_y = \begin{bmatrix}\hat{M}_{x_r} & \hat{M}_{x_e}\end{bmatrix}\begin{bmatrix}x_r\\ \hat{x}_e\end{bmatrix} + \begin{bmatrix}\hat{M}_{u_r} & \hat{M}_{u_e}\end{bmatrix}\begin{bmatrix}u_r\\ u_e\end{bmatrix} \quad (4)$$

where $\hat{M}_x \in \Re^{1 \times n_x}$ and $\hat{M}_u \in \Re^{1 \times n_u}$ are unknown but presumptive.

B. Disturbance Augmented Model

The gust-disturbed dynamics of the flexible wing GTM can be modeled as

$$\dot{x}(t) = Ax(t) + Bu(t) + d(t) \quad (5)$$

$$y(t) = Cx(t) + Du(t) + Ed(t) \quad (6)$$

$$M_y(t) = M_x x(t) + M_u u(t) + M_d d(t). \quad (7)$$

This representation, which was justified in [12], has $d(t) \in \Re^{n_x}$ directly impact the state update $\dot{x}$ without passing through the A or B matrix. Note that $d(t)$ also affects the output vector after multiplication with $E \in \Re^{n_y \times n_x}$ in $y(t)$ and $M_d \in \Re^{1 \times n_x}$ in $M_y(t)$. The matrices E and M_d are unknown. This disturbance structure makes the estimation of $d(t)$ very difficult or even impossible in some conditions.

In [13], the authors prove the existence of an equivalent input disturbance (EID) that generates an output effect identical to the actual disturbance. The concept has since been successfully applied to many robust disturbance observation and compensation applications [14]-[16]. With EID results, we can assume that the disturbance is imposed only on the control input channel such that equations (5) - (7) can be replaced with

$$\dot{x}_{EID}(t) = Ax_{EID}(t) + B\left(u(t) + d_{EID}(t)\right) \quad (8)$$

$$y(t) = Cx_{EID}(t) + D\left(u(t) + d_{EID}(t)\right) \quad (9)$$

$$M_y(t) = M_x x_{EID}(t) + M_u\left(u(t) + d_{EID}(t)\right) \quad (10)$$

where $d_{EID}(t) = [d_{r,EID}^T \; d_{e,EID}^T]^T \in \Re^{n_u}$ is an equivalent input disturbance and $x_{EID}(t) \in \Re^{n_x}$ is an internal state variable of the new system model that is different from $x(t)$.

III. GUST LOAD ALLEVIATION CONTROL

A. Rigid State Control

As previously discussed, the state of the flexible wing GTM is divided into two parts, x_r and x_e. The control of x_r is critical for trajectory-level flight control. Therefore, it is necessary to independently design an x_r controller to meet flight objectives. A standard LQR control design is used to determine an appropriate rigid state controller, and its formulation is based on the simplified model

$$\dot{x}_r = A_{rr}x_r + B_{rr}u_r \quad (11)$$

which is used to generate the gain matrix K_r for

$$u_r = K_r x_r. \quad (12)$$

Note that in this formulation the x_r controller only regulates x_r and does not include the necessary servo mechanism for command tracking. This is sufficient for an aircraft assumed to be at cruising conditions where there is a need to maintain the nominal trimmed state values only. Equation (11) also disregards the effect of x_e and u_e in the x_r update. However, the omission is a tolerable approximation as the scale of x_e is small compared to x_r at flight conditions safely below flutter.

B. Elastic State Control

Since u_r is a command independently generated according to equation (12), the only remaining input channel for GLA is u_e. However, two independent goals (M_y reduction, x_e regulation) must be achieved simultaneously through the use of u_e for successful GLA. One possible solution is to design a controller for each purpose separately and combine the commands into a single signal as shown in Fig. 2. The

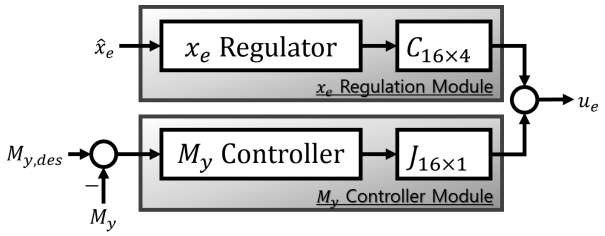

Fig. 2. Concept diagram of elastic state controller. Parallel control design is applied that each controller operates only to achieve its own goal.

following subsections show how the respective controllers are designed.

1) x_e regulator design: A standard LQR formulation has been adopted for x_e regulation. For LQR gain calculation, the dynamic equation

$$\dot{x}_e = A_{ee}x_e + B_{ee}u_{e,x_e} \tag{13}$$

$$u_{e,xe} = \Gamma u^{chev}_{e,x_e} \tag{14}$$

is used where only elastic state and input components are selected in equation (1) in a manner similar to the derivation of K_r in equations (11) and (12). The quantity $\Gamma \in \Re^{16\times4}$ is a cubic Chevyshev polynomial matrix with

$$\Gamma u^{chev}_{e,x_e} = \begin{bmatrix}\beta_1 & \beta_2 & \cdots & \beta_i & \cdots & \beta_{15} & \beta_{16}\end{bmatrix}^T \tag{15}$$

$$\beta_i = c_0 + c_1 k + c_2(2k^2-1) + c_3(4k^3-3k) \tag{16}$$

where $k = \frac{i-1}{n-1}, i = 1, 2, \cdots, 16, n = 16$. The components c_j with $j = 0, 1, 2, 3$ form a set of virtual control inputs $u^{chev}_{e,x_e} = [c_0\ c_1\ c_2\ c_3]^T$. Since the cubic Chevyshev polynomial is a shape function with four coefficients that have a mathematically smooth curve, it helps produce a smooth trailing edge profile with flap deflections that are less likely to violate mechanical constraints on relative angles between adjacent flaps [8]. From equations (13) and (14),

$$u^{chev}_{e,x_e} = K_e\hat{x}_e \tag{17}$$

is derived where $K_e \in \Re^{4\times n_{x_e}}$. We use $\hat{x}_e$ instead of x_e in actual signal generation due to the unmeasurable properties of elastic states.

2) M_y controller design: As discussed earlier, the DOB algorithm is selected to add robustness to the GLA design. However, the application of DOB to a non-SISO system is quite limited because DOB is exclusively designed for linear single-input single-output (SISO) systems [17]. Therefore, we choose to introduce a new component called $J \in \Re^{16\times1}$, which is a user-selected gain matrix that maps the scalar M_y controller output to each control surface, to make the plant as a SISO system. With a well chosen J matrix, the scalar M_y control command becomes a sixteen flap control input vector. In this paper, a simple PID controller is adopted for M_y control and is placed in the position of the 'M_y Controller' block in Fig. 2. The overall controller structure for both the u_r and u_e commands is shown in Fig. 3. The 'M_y-PID' block generates a signal α based on the error between $M_{y,des}$ and measured M_y. With α and the DOB signal ϵ, a scalar u_{e,M_y} signal is generated. Multiplying by J, the signal becomes a vector of sixteen control inputs, symbolized by $u_{e,J}$. The x_e regulation control input u_{e,x_e} is added to $u_{e,J}$ for final control input u_e generation. We assume that $d_{e,EID}$ is added to u_e such that it contaminates the original signal, making the imaginary signal ζ as a final plant control input.

3) Disturbance Observer: The goal of the DOB is to assist in making the plant behave as the nominal model, even when disturbed. In order to achieve robustness, we calculate the best ϵ that represents the estimated disturbance affecting the plant. For good ϵ calculation, δ should be a good representation of ζ in the frequency region where the disturbance is concentrated. However, in our DOB design we join the ϵ and α signals before the mapping provided by the J matrix. Therefore, we should determine a δ that is more like a representation of $J^*\hat{\zeta}$ rather than $\hat{\zeta}$ where $JJ^* \approx I$.

Among the many input-output relationships, we define Λ_p as a transfer function capturing the $u_{e,M_y} \rightarrow M_y$ relationship. Since we already discussed the x_r controller and x_e regulator, we are now able to derive the state-space representation of $\bar{\Lambda}_p$ from equations (1) and (4) as

$$\dot{\bar{x}} = A\bar{x} + B_r u_r + B_e(u_{e,x_e} + u_{e,J}) \tag{18}$$

$$M_y = M_x\bar{x} + M_{ur}u_r + M_{ue}(u_{x,x_e} + u_{e,J}). \tag{19}$$

Note that we already know the state feedback control laws to be used for u_r and u_{e,x_e} as given in equations (12), (14) and (17). The $\bar{*}$ notation represents the nominal model of the plant while B_r and B_e represent $[B_{rr}\ B_{er}]^T$ and $[B_{re}\ B_{ee}]^T$ respectively. Therefore, we can rewrite equations (18) and (19) as

$$\dot{\bar{x}} = \bar{A}\bar{x} + \bar{B}u_{e,My} \tag{20}$$

$$M_y = \bar{M}_x\bar{x} + \bar{M}_u u_{e,M_y} \tag{21}$$

where

$$\bar{A} = A + B\begin{bmatrix}K_r & 0\\ 0 & \Gamma K_e\end{bmatrix}, \bar{B} = B_e J \tag{22}$$

$$\bar{M}_x = M_x + M_u\begin{bmatrix}K_r & 0\\ 0 & \Gamma K_e\end{bmatrix}, \bar{M}_u = M_{ue}J. \tag{23}$$

The estimation of $J^*\zeta$ is performed by $\bar{\Lambda}_p^{-1}$. By putting the sensor-measured M_y signal through $\bar{\Lambda}_p^{-1}$, we can estimate $J^*\zeta$. To prevent instability in $J^*\zeta$ estimation due to the the improper and non-minimum phase structure of $\bar{\Lambda}_p^{-1}$, a Q-filter Q_1 is carefully selected to combine with $\bar{\Lambda}_p^{-1}$ to ensure stable estimation and accurate output in the designated frequency region. The filter Q_2 is designed to match the phase during the ϵ calculation. A detailed design procedure of the Q-filters for our plant will be discussed in a later section.

When δ is calculated accurately, we establish the following lemma.

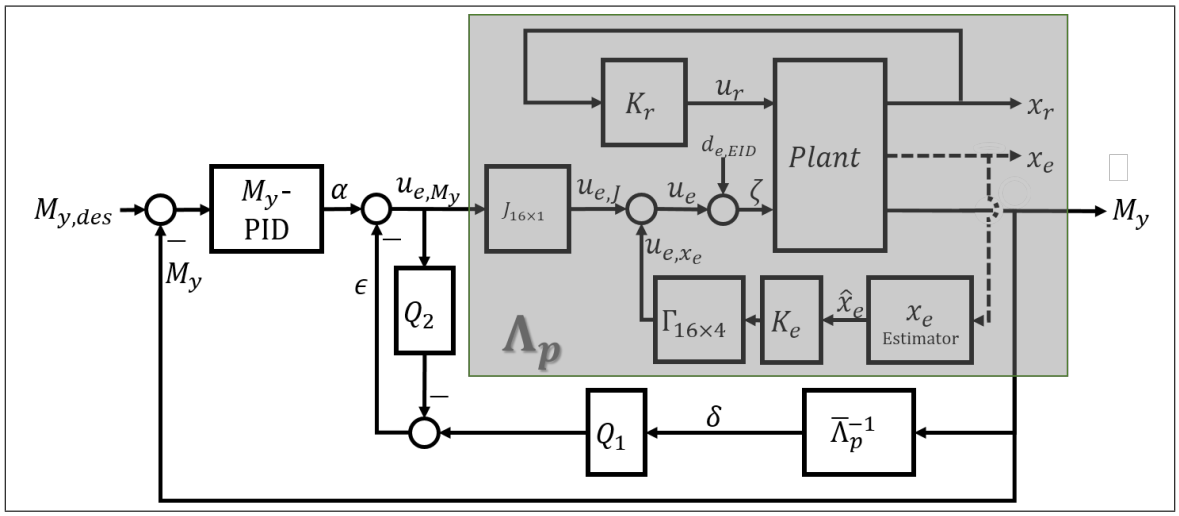

Fig. 3. Schematic diagram of a robust DOB-based GLA control structure. SISO transfer function Λ_p between u_{e,M_y} and M_y is established through the loop-closing of x_r and x_e with LQR controller.

Lemma 1: If δ provides $J^*\zeta$ estimation accurately within the specified frequency region, then $\zeta \approx J\alpha$.

Proof: In Fig. 3, $\zeta = u_e + d_{e,EID}$. The u_e signal is the sum of $u_{e,J}$ and u_{e,x_e}. Therefore, $\zeta = u_{e,J} + u_{e,x_e} + d_{e,EID}$. However, since $u_{e,J}$ is same as Ju_{e,M_y}, ζ becomes $Ju_{e,M_y} + u_{e,x_e} + d_{e,EID}$. It can be rewritten as $\zeta = J(\alpha - \epsilon) + u_{e,x_e} + d_{e,EID}$ where $u_{e,M_y} = \alpha - \epsilon$. With proper Q_1 and Q_2 design, $\epsilon = (Q_1\delta - Q_2u_{e,M_y}) \approx (\delta - u_{e,M_y})$ in the designated frequency region. Then $\zeta \approx J(\alpha - (\delta - u_{e,M_y})) + u_{e,x_e} + d_{e,EID}$ also in the designated frequency region. Since $\delta = J^*\hat{\zeta}$, the equation becomes $\zeta \approx J(\alpha - J^*\hat{\zeta} + u_{e,M_y}) + u_{e,x_e} + d_{e,EID}$ where $\hat{\zeta} = \hat{u}_e + \hat{d}_{e,EID}$. Therefore $\zeta \approx J(\alpha - J^*(\hat{u}_e + \hat{d}_{e,EID}) + u_{e,M_y}) + u_{e,x_e} + d_{e,EID}$. Recalling that $JJ^* \approx I$, the equation becomes $\zeta \approx J\alpha + ((Ju_{e,M_y} + u_{e,x_e}) - \hat{u}_e) + (d_{e,EID} - \hat{d}_{e,EID})$. Also recalling that $u_e = Ju_{e,M_y} + u_{e,x_e}$, the final form of the equation is $\zeta \approx J\alpha + (u_e - \hat{u}_e) + (d_{e,EID} - \hat{d}_{e,EID})$, or $\zeta \approx J\alpha$. ■

Lemma 1 proves the robustness of the proposed controller by showing that the final control input ζ remains similar to the controller input $J\alpha$ even with disturbance $d_{e,EID}$.

Now, we can regulate the disturbed M_y by selecting $M_{y,des} = 0$. However, robustness of the controller is based on good Q-filter design. By designing Q-filter properly, we need to secure both stability and performance of the disturbance estimation process simultaneously. In the next section, we discuss a Q-filter design methodology to satisfy both goals at the same time.

IV. Q-FILTER DESIGN

In this section, we design a Q-filter that satisfies both the stability and performance goals of the disturbance estimation process. Deductive DOB stability analysis for the GTM is avoided due to the complexity of our system. Instead, we provide a dedicated Q-filter design procedure for our case and provide stability analysis in a later section. The filter aims to overcome issues including instability, non-minimum phase behavior, and improperness during the disturbance estimation process. Consideration of these issues during Q-filter design results in structure involving components $Q_{1,A}$ and $Q_{1,B}$ where

$$Q_1 = Q_{1,A}Q_{1,B}. \tag{24}$$

Throughout this paper, we assume that $Q_2 = Q_1$, because the role of Q_2 is to delay the phase of the u_{e,M_y} signal appropriately to match the phase with $Q_1\delta$ signal, and the $Q_2 = Q_1$ setting is the easiest way to satisfy it [19].

A. Unstable and non-minimum phase systems

The first process in Q-filter design is stabilizing the nominal model inverse. Once J has been selected, we need to determine if any (RHP) poles or zeros exist that make the system unstable or non-minimum phase. If we find RHP poles in $\bar{\Lambda}_p$, then we need to reselect the J matrix since the plant with current J is fundamentally unstable. After proper J selection without any RHP poles, our next task is to make sure that the system is minimum phase. This is required to prevent unstable δ estimation since non-minimum phase zeros in $\bar{\Lambda}_p$ become unstable RHP poles in $\bar{\Lambda}_p^{-1}$. As a solution, we choose to design a Q-filter that moves any existing RHP zeros of $\bar{\Lambda}_p$ to the symmetric LHP location where the distance from the imaginary axis is equal but the sign is reversed. This process changes the phase response but results in the same magnitude response. For example, when $\bar{\Lambda}_p$ contains ν number of RHP zeros $z_{i,rhp} > 0, i = 1, \cdots, \nu$, we design the Q-filter as

$$Q_{1,A} = \frac{\prod_{i=1}^{\nu}(s - z_{i,rhp})}{\prod_{i=1}^{\nu}(s + z_{i,rhp})} \tag{25}$$

such that the relative degree of the system remains the same, but the locations of the RHP zeros move to the symmetric LHP positions.

B. Improper systems

Once we ensure the system is minimum-phase, our next goal is to make the system proper. Since $\bar{\Lambda}_p$ is a proper system, it is obvious that $\bar{\Lambda}_p^{-1}$ becomes improper. Also, it is well known that the Q-filter should be a low pass filter to provide the desired performance [20]. To solve this problem, a Butterworth filter structure is adopted. The Butterworth filter is a low pass filter showing flat magnitude response until the designated cutoff frequency. Therefore, it preserves the magnitude response of $\bar{\Lambda}_p^{-1}$ until the designated cutoff frequency. We choose to make $Q_1\bar{\Lambda}_p^{-1}$ have a relative degree of two. If we define γ as the relative degree of $\bar{\Lambda}_p$, the Q-filter should be

$$Q_{1,B} = (\gamma + 2)^{th} \ order \ Butterworth \ filter. \tag{26}$$

Now, the only remaining aspect of Q-filter design is choosing a cutoff frequency for the Butterworth filter that balances stability and performance of the DOB in GLA. For analysis to select the cut-off frequency, we adopt the concept used in [18], where a cutoff frequency designing criteria is formed from time delay observations between the nominal and actual plant. For similar analysis, we assume that the actual plant can be modeled as

$$\Lambda_p(s) = e^{-sT_d}\tilde{\Lambda}_p(s) \tag{27}$$

where T_d represents observed response time delay between the nominal and actual plant. $\tilde{\Lambda}_p(s)$ is the newly defined nominal model in $Q_{1,B}$ design process, expressed as

$$\tilde{\Lambda}_p(s) = Q_{1,A}^{-1}\bar{\Lambda}_p(s). \tag{28}$$

The reason for defining the new nominal model is to treat $Q_{1,A}$ as part of the nominal model during the $Q_{1,B}$ design process, since $Q_{1,B}$ is the only element that matches the definition of the Q-filter in [18]. Next step, we express the error between $\Lambda_p(s)$ and $\tilde{\Lambda}_p(s)$ in the form of a multiplicative perturbation as

$$\Lambda_p(s) = \tilde{\Lambda}_p(s)(1 + \Delta(s)) \tag{29}$$

where

$$\Delta(s) = e^{-sT_d} - 1. \tag{30}$$

We then enforce the requirement

$$||\Delta \cdot Q_1||_\infty < 1, \tag{31}$$

which is a stability condition based on a small gain theorem [20][21], and set the cutoff frequency only by finding T_d.

V. GTM SIMULATION RESULTS

In this section, we present the GTM simulation results with proposed GLA algorithm. The simulation is based on equation (5) $\sim$ (7) and the gust disturbance $d(t)$ is generated from a random signal using the Von Karman gust model [22]. Three simulations with different J choices are conducted. The candidate J matrices are

- $J_1 = [[1\ 1\ \cdots\ 1\ 1]_{1\times 16}]^T$
- $J_2 = [[0\ .1\ .2\ \cdots\ .9\ 1\ .9\ \cdots\ .5]_{1\times 16}]^T$

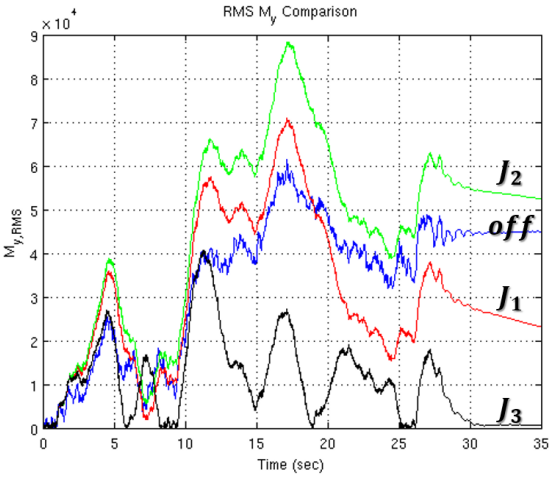

Fig. 4. Comparison of root mean square (RMS) values of wing root bending moment (M_y) for each J selection.

- $J_3 = [[-1\ 1\ 1\ \cdots\ 1\ 2\ 2]_{1\times 16}]^T$.

J_1 corresponds to operation of all flaps as a single large flap. J_2 emphasizes flap motion in a specific region where contribution to wing root bending moment is greatest. J_3 is similar to J_1, but has the first flap moving in opposition. The counter motion of the first flap in J_3 is to help offset the loss of lift force during the M_y minimization process, where wing root bending moment reduction decreases the overall lift generation of the wing. Outboard flap movement has been doubled to increase control efficiency. Fig. 4 shows the comparative M_y regulation result for each J selection. The 'off' mode refers to the case without x_e regulator or M_y controller but with x_r controller. Among the three examples, we found that J_3 shows the best performance. Recall that J is a tuning parameter where any number of options exist. Since J_3 has shown the best performance among the limited options we explored, we select J_3 for a case study to demonstrate filter design process and analyze the proposed

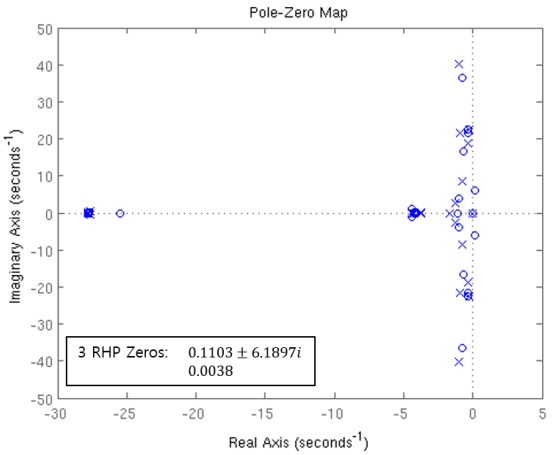

Fig. 5. Pole/Zero map of $\bar{\Lambda}_p$ with J_3.

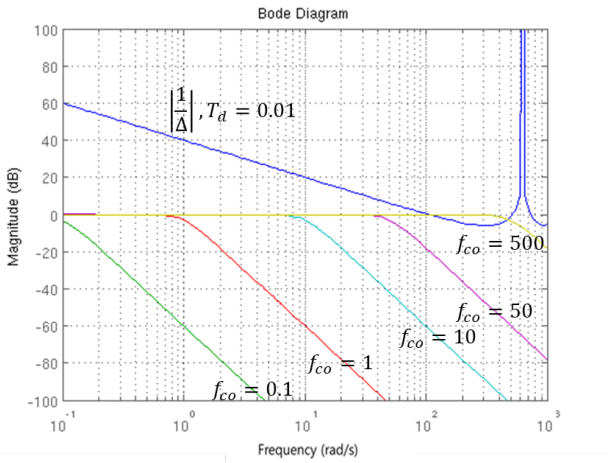

Fig. 6. Bode magnitude diagram of $1/||\Delta||$ (blue line on the top side) and $Q_{1,B}$ (rest of the line) with various cutoff frequencies.

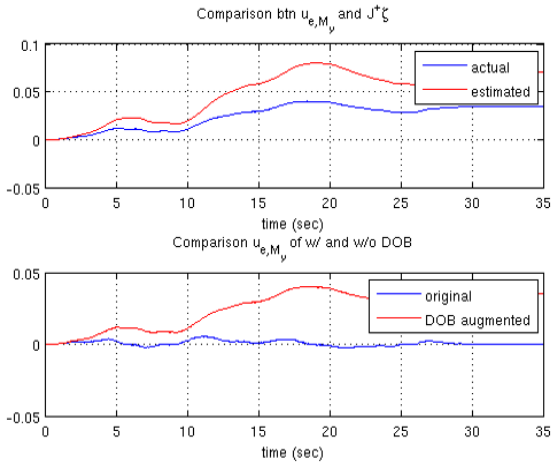

Fig. 8. Comparison of control inputs between actual and estimated values (top), before and after applying DOB algorithm (bottom).

control structure.

A. Cut-off frequency selection

In a pole/zero analysis, we found that three zeros of $\bar{\Lambda}_p$ are placed at $0.1103 \pm 6.1897i$ and 0.0038 with J_3 while no RHP poles are found. See Fig. 5 for the pole/zero map. Based on equation (25), $Q_{1,A}$ is designed to relocate the non-minimum phase zeros from the RHP to the LHP. Then, we select a 3^{rd} order Butterworth filter based on equation (26) since the relative degree of the system in this case is one. From a unit step response comparison between $\tilde{\Lambda}_p(s)$ and $\Lambda_p(s)$, we found that $T_d \approx 0.01$. Using equation (31), we derive the following inequality

$$||Q_1|| < \frac{1}{||\Delta||} \tag{32}$$

where satisfaction of the inequality constraint during Q-filter design automatically guarantees system stability. The cutoff frequency is selected by analyzing the Bode magnitude plot in Fig. 6. Equation (32) is satisfied by selecting a Q-filter design with magnitude lower than that of $1/||\Delta||$.

By overlaying several Q-filter Bode magnitude plots, we estimate that the cutoff frequency stability threshold is somewhere between 50 Hz and 500 Hz. As the $||Q_1||$ plot approaches $1/||\Delta||$, the DOB performance increases, but stability of the overall system decreases. Moving the other way, stability of the overall system improves, but DOB performance decreases. We select 50Hz as a cutoff frequency to provide adequate stability while not sacrificing too much DOB performance.

B. Simulation results

In this subsection, we provide GTM simulation results with the GLA controller. Fig. 7 shows the VCCCTEF command generated by the GLA controller in time series. Note that the inboard flap moves in the opposite direction from the other flaps as intended by the J_3 design. The effect of the conversely moving the first flap on lift generation can be seen indirectly in Fig. 9. This figure shows the comparison of J_1 usage (left) and J_3 usage (right). In this comparison,

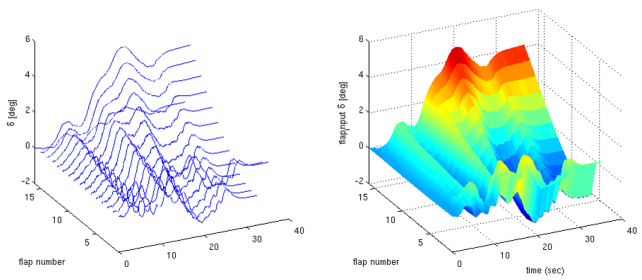

Fig. 7. A graph showing changes in VCCTEF control input over time. Wireframe representation (left) and plane representation (right).

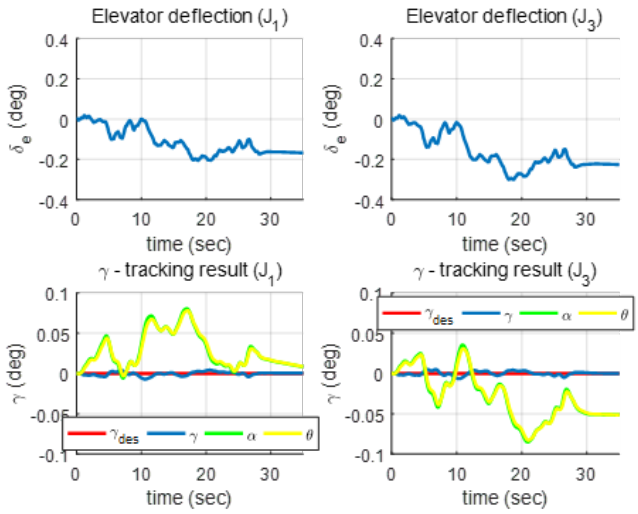

Fig. 9. A comparison of elevator deflection, flight path angle, angle of attack and pitch angle in J1 (left) and J3 (right) modes.

both elevator deflection and flight path tracking (γ-tracking) show almost the same performance. However, unlike the case of J_1 where the pitch angle converges to a value close to zero, J_3 converges to a negative value. This indicates that additional lift force is generated during the GLA control process when J_3 is used. The rigid state controller pitches the aircraft nose down to regulate the increased lift force and maintain a flight path angle of zero. It is clear that the conversely moving first flap makes a contribution to lift force generation while the other flaps reduce lift force during M_y minimization control. The reducing effect of M_y control on lift force can be confirmed by J_1 simulation with batched flap motion. In this case the rigid state controller struggles to keep zero flight path angle while attempting to pitch up to generate additional lift in response to the counteractive action of the M_y controller. The J_3 simulation shows that the main source of lift force is concentrated at the wing root. The reduction in lift force over the outer wing is a useful feature to exploit for M_y minimization since the outboard portion of the wing has a longer moment arm length than the inboard portion and generates a larger wing root bending moment even with a small control action.

The effect of the DOB algorithm in GLA command generation can be observed in Fig. 8. The blue line in the upper graph represents the actual u_{e,M_y} command. Meanwhile, the red line represents $\delta = J^* \hat{\zeta}$ which is the estimated command calculated from M_y measurement data. The gap between two lines is an estimated EID signal ϵ. We can subtract ϵ from α to generate u_{e,M_y} which contains the disturbance compensation signal. The lower graph shows the comparison between α and u_{e,M_y}, the control signal before and after DOB is applied. We can see that u_{e,M_y} (red line) shows a larger command signal compared to α (blue line) since ϵ is added to α.

VI. CONCLUSION

In this paper, we described the structure of a novel GLA control algorithm incorporating a disturbance observer and demonstrated the performance of a DOB-GLA controller that encounters an unknown gust disturbance. By adapting the equivalent input disturbance concept to our needs, we were able to formulate a control design that alleviates aeroservoelastic disturbances and reduces wing root bending moment by generating rigorously calculated additional control input signals. To achieve the multiple (and sometimes counteractive) goals of the GLA system, a parallel controller structure is introduced. The DOB algorithm is adopted for calculating the EID signal and compensating for the disturbance through the M_y controller. A Q-filter design has been presented to satisfy both adequate stability and performance. Simulation results are shown to verify the feasibility of the algorithm and to illustrate various design possibilities.

However, this study does not explore a large parameter space for many of the design choices. Notably, very few option for the command mapping matrix J are investigated, and the choice of J is likely far from optimal. Therefore, a methodology to find an optimal J matrix should be developed in further research.

REFERENCES

[1] Nguyen, Nhan, et al. "Development of Variable Camber Continuous Trailing Edge Flap for Performance Adaptive Aeroelastic Wing." SAE 2015 AeroTech Congress and Exhibition. (2015).

[2] Norman, D. C. "Practical gust load alleviation and flutter suppression control laws based on a LQG methodology." (1981).

[3] Aouf, Nabil, Benoit Boulet, and Ruxandra Botez. "H/sub 2/and H/sub/spl infin//-optimal gust load alleviation for a flexible aircraft." American Control Conference, 2000. Proceedings of the 2000. Vol. 3. IEEE, 2000.

[4] Mukhopadhyay, V., J. R. Newsom, and I. Abel. "Reduced-order optimal feedback control law synthesis for flutter suppression." Journal of Guidance, Control, and Dynamics 5.4 (1982): 389-395.

[5] Nguyen, Nhan T., and Kelley E. Hashemi. "Performance Optimizing Adaptive Control with Time-Varying Reference Model Modification." Report No. ARC-E-DAA-TN42886. Available from NTRS. (2017).

[6] Nguyen, Nhan T., et al. "Performance Optimizing Multi-Objective Adaptive Control with Time-Varying Model Reference Modification." AIAA Guidance, Navigation, and Control Conference. (2017).

[7] Aouf, Nabil, Benoit Boulet, and R. M. Botez. "Robust gust load alleviation for a flexible aircraft." Canadian Aeronautics and Space Journal 46.3 (2000): 131-139.

[8] Cook, Robert G., Rafael Palacios, and Paul Goulart. "Robust gust alleviation and stabilization of very flexible aircraft." AIAA journal (2013).

[9] Shim, Hyungbo, Nam Hoon Jo, and Young-Ik Son. "A new disturbance observer for non-minimum phase linear systems." American Control Conference, 2008. IEEE, 2008.

[10] Shim, Hyungbo, et al. "Yet another tutorial of disturbance observer: robust stabilization and recovery of nominal performance." Control Theory and Technology 14.3 (2016): 237-249.

[11] Nguyen, Nhan, and Ezra Tal. "A Multi-Objective Flight Control Approach for Performance Adaptive Aeroelastic Wing." 56th AIAA/ASCE/AHS/ASC Structures, Structural Dynamics, and Materials Conference. 2015.

[12] Nguyen, Nhan, et al. "Multi-Objective Flight Control for Drag Minimization and Load Alleviation of High-Aspect Ratio Flexible Wing Aircraft." AIAA Guidance, Navigation, and Control Conference. (2017).

[13] She, Jin-Hua, et al. "Improving disturbance-rejection performance based on an equivalent-input-disturbance approach." IEEE Transactions on Industrial Electronics 55.1 (2008): 380-389.

[14] Liu, Rui-Juan, et al. "Disturbance rejection for time-delay systems based on the equivalent-input-disturbance approach." Journal of the Franklin Institute 351.6 (2014): 3364-3377.

[15] Wu, Min, et al. "Design of equivalent-input-disturbance estimator using a generalized state observer." Journal of Control Theory and Applications 11.1 (2013): 74-79.

[16] She, Jinhua, et al. "Global stabilization of 2-DOF underactuated mechanical systemsan equivalent-input-disturbance approach." Nonlinear Dynamics 69.1 (2012): 495-509.

[17] Shahruz, S. M. "Active vibration suppression in multi-degree-of-freedom systems by disturbance observers." Journal of vibration and control 15.8 (2009): 1207-1228.

[18] Kempf, Carl J., and Seiichi Kobayashi. "Disturbance observer and feedforward design for a high-speed direct-drive positioning table." IEEE Transactions on control systems Technology 7.5 (1999): 513-526.

[19] Shim, Hyungbo, and Nam H. Jo. "An almost necessary and sufficient condition for robust stability of closed-loop systems with disturbance observer." Automatica 45.1 (2009): 296-299.

[20] Sariyildiz, Emre, and Kouhei Ohnishi. "A guide to design disturbance observer." Journal of Dynamic Systems, Measurement, and Control 136.2 (2014): 021011.

[21] Lee, Seung Jae, et al. "Robust acceleration control of a hexarotor UAV with a disturbance observer." Decision and Control (CDC), 2016 IEEE 55th Conference on. IEEE, 2016.

[22] Tal, Ezra, and Nhan Nguyen. "Unsteady Aeroservoelastic Modeling of Flexible Wing Generic Transport Aircraft with Variable Camber Continuous Trailing Edge Flap." 33rd AIAA Applied Aerodynamics Conference. 2015.